Superconducting qubit–oscillator circuit beyond the ultrastrong-coupling regime

Fumiki Yoshihara[1]★†, Tomoko Fuse[1]★†, Sahel Ashhab[2]★, Kosuke Kakuyanagi[3], Shiro Saito[3] and Kouichi Semba[1]★

The interaction between an atom and the electromagnetic field inside a cavity[1-6] has played a crucial role in developing our understanding of light–matter interaction, and is central to various quantum technologies, including lasers and many quantum computing architectures. Superconducting qubits[7,8] have allowed the realization of strong[9,10] and ultrastrong[11-13] coupling between artificial atoms and cavities. If the coupling strength g becomes as large as the atomic and cavity frequencies (Δ and ω_o, respectively), the energy eigenstates including the ground state are predicted to be highly entangled[14]. There has been an ongoing debate[15-17] over whether it is fundamentally possible to realize this regime in realistic physical systems. By inductively coupling a flux qubit and an LC oscillator via Josephson junctions, we have realized circuits with g/ω_o ranging from 0.72 to 1.34 and $g/\Delta \gg 1$. Using spectroscopy measurements, we have observed unconventional transition spectra that are characteristic of this new regime. Our results provide a basis for ground-state-based entangled pair generation and open a new direction of research on strongly correlated light–matter states in circuit quantum electrodynamics.

We begin by describing the Hamiltonian of each component in the qubit–oscillator circuit, which comprises a superconducting flux qubit and an LC oscillator inductively coupled to each other by sharing a tunable inductance L_c, as shown in the circuit diagram in Fig. 1a.

The Hamiltonian of the flux qubit can be written in the basis of two states with persistent currents flowing in opposite directions around the qubit loop[18], $|L\rangle_q$ and $|R\rangle_q$, as $\mathcal{H}_q = -\hbar(\Delta\sigma_x + \varepsilon\sigma_z)/2$, where $\hbar\Delta$ and $\hbar\varepsilon = 2I_p\Phi_0(n_{\phi q} - n_{\phi q0})$ are the tunnel splitting and the energy bias between $|L\rangle_q$ and $|R\rangle_q$, I_p is the maximum persistent current, and $\sigma_{x,z}$ are Pauli matrices. Here, $n_{\phi q}$ is the normalized flux bias through the qubit loop in units of the superconducting flux quantum, $\Phi_0 = h/2e$, and $n_{\phi q0} = 0.5 + k_q$, where k_q is the integer that minimizes $|n_{\phi q} - n_{\phi q0}|$. The macroscopic nature of the persistent-current states enables strong coupling to other circuit elements. Another important feature of the flux qubit is its strong anharmonicity: the two lowest energy levels are well isolated from the higher levels.

The Hamiltonian of the LC oscillator can be written as $\mathcal{H}_o = \hbar\omega_o(\hat{a}^\dagger\hat{a} + 1/2)$, where $\omega_o = 1/\sqrt{(L_0 + L_{qc})C}$ is the resonance frequency, L_0 is the inductance of the superconducting lead, $L_{qc}(\simeq L_c)$ is the inductance across the qubit and coupler (see Supplementary Section 2), C is the capacitance, and $\hat{a}$ ($\hat{a}^\dagger$) is the oscillator's annihilation (creation) operator. Figure 1b shows a laser microscope image of the lumped-element LC oscillator, where

L_0 is designed to be as small as possible to maximize the zero-point fluctuations in the current $I_{zpf} = \sqrt{\hbar\omega_o/2(L_0 + L_{qc})}$ and hence achieve strong coupling to the flux qubit, while C is adjusted so as to achieve a desired value of ω_o. The freedom of choosing L_0 for large I_{zpf} is one of the advantages of lumped-element LC oscillators over coplanar-waveguide resonators for our experiment. Another advantage is that a lumped-element LC oscillator has only one resonant mode. Together with the strong anharmonicity of the flux qubit, we can expect that our circuit will realize the Rabi model[19-22], which is one of the simplest possible quantum models of qubit–oscillator systems, with no additional energy levels in the range of interest.

The coupling Hamiltonian can be written as[9] $\mathcal{H}_c = \hbar g\sigma_z(\hat{a} + \hat{a}^\dagger)$, where $\hbar g = MI_pI_{zpf}$ is the coupling energy and $M(\simeq L_c)$ is the mutual inductance between the qubit and the LC oscillator. Importantly, a Josephson-junction circuit is used as a large inductive coupler[23] (Fig. 1c), which together with the large I_p and I_{zpf} pushes the device into the regime where g is comparable to or larger than both Δ and ω_o. This regime is sometimes referred to as deep strong coupling[24].

The total Hamiltonian of the circuit is then given by

$$\mathcal{H}_{total} = -\frac{\hbar}{2}(\Delta\sigma_x + \varepsilon\sigma_z) + \hbar\omega_o\left(\hat{a}^\dagger\hat{a} + \frac{1}{2}\right) + \hbar g\sigma_z(\hat{a} + \hat{a}^\dagger) \quad (1)$$

Nonlinearities in the coupler circuit lead to higher-order terms in $(\hat{a} + \hat{a}^\dagger)$. The leading-order term can be written as $C_{A2}\hbar g(\hat{a} + \hat{a}^\dagger)^2$ and is known as the A^2 term[15] in atomic physics. Since this A^2 term can be eliminated from $\mathcal{H}_{total}$ by a variable transformation (see Methods), we do not explicitly keep it and instead use equation (1) for our data analysis.

Spectroscopy was performed by measuring the transmission spectrum through a coplanar transmission line that is inductively coupled to the LC oscillator (see Supplementary Section 3). For a systematic study of the g dependence, five flux bias points in three circuits were used. Circuit II is designed to have larger values of g than the other two, and circuits I and II are designed to have smaller values of Δ than circuit III. Figure 2a–d shows normalized amplitudes of the transmission spectra $|S_{21}(\omega_p)|/|S_{21}(\omega_p)|_{max}$ from circuits I and II as functions of the flux bias ε and probe frequency ω_p (see also Supplementary Fig. 5a–d). Characteristic patterns resembling masquerade masks can be seen around $\varepsilon = 0$. At each value of ε, the spectroscopy data were fitted with Lorentzians to obtain the frequencies ω_{ij} of the transitions $|i\rangle \rightarrow |j\rangle$, where the indices i and j label the energy eigenstates according to their order in the energy-level ladder, with the index 0 denoting the ground

[1]National Institute of Information and Communications Technology, 4-2-1, Nukui-Kitamachi, Koganei, Tokyo 184-8795, Japan. [2]Qatar Environment and Energy Research Institute, Hamad Bin Khalifa University, Qatar Foundation, PO Box 5825, Doha, Qatar. [3]NTT Basic Research Laboratories, NTT Corporation, 3-1 Morinosato-Wakamiya, Atsugi, Kanagawa 243-0198, Japan. †These authors contributed equally to this work. *e-mail: fumiki@nict.go.jp; tfuse@nict.go.jp; sashhab@qf.org.qa; semba@nict.go.jp
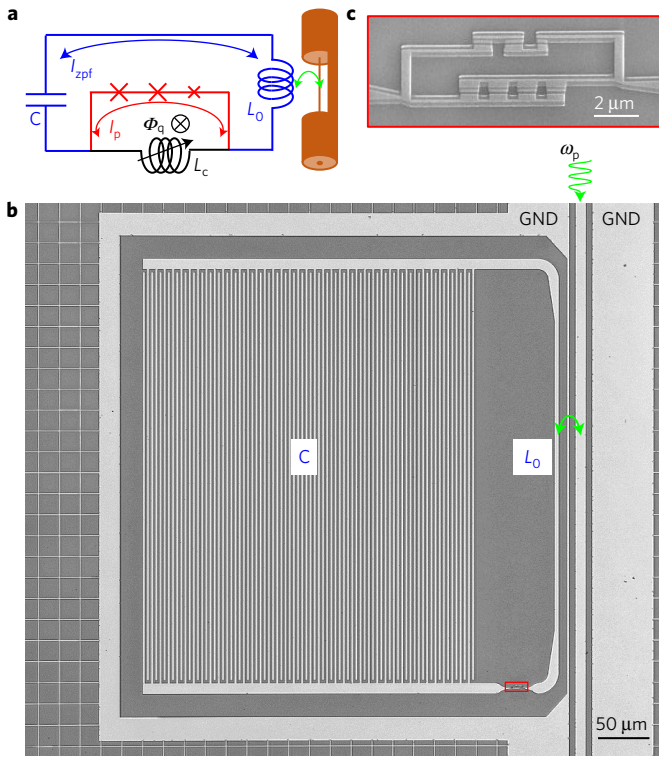
Figure 1 | Superconducting qubit–oscillator circuit. a, Circuit diagram. A superconducting flux qubit (red and black) and a superconducting LC oscillator (blue and black) are inductively coupled to each other by sharing a tunable inductance (black). **b**, Laser microscope image of the lumped-element LC oscillator inductively coupled to a coplanar transmission line. **c**, Scanning electron microscope image of the qubit and the coupler junctions located at the red rectangle in image **b**. The coupler, consisting of four parallel Josephson junctions, is tunable via the magnetic flux bias through its loops (see Supplementary Sections 1 and 2, and Supplementary Fig. 1).

state. Theoretical fits to ω_{ij} were obtained by diagonalizing $\mathcal{H}_{\text{total}}$, treating Δ, ω_{o} and g as fitting parameters. The obtained parameters are shown in Table 1. The calculated transition frequencies ω_{ij}^{cal} are superimposed on the measured transmission spectra. As g increases, the anticrossing gap between the qubit and the oscillator frequencies at $\varepsilon \simeq \pm\omega_{\text{o}}$ becomes smaller and the signal from the $|1\rangle \to |3\rangle$ transition gradually transforms from a W shape to a Λ shape in the range $|\varepsilon| \lesssim \omega_{\text{o}}$. These features are seen in both the experimental data and the theoretical calculations, with good agreement between the data and the calculations. Note that ω_{o} depends on the qubit state and ε via L_{qc}, which results in the broad V shape seen in the spectra (see Supplementary Section 2).

To capture signals from more transitions, the transmission spectra in a wider ω_{p} range and a smaller ε range were measured,
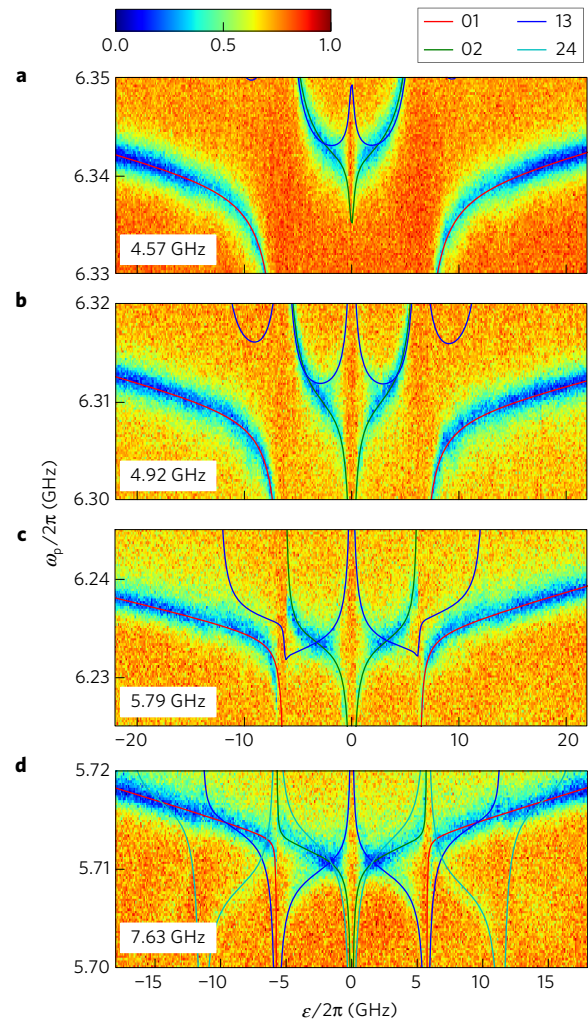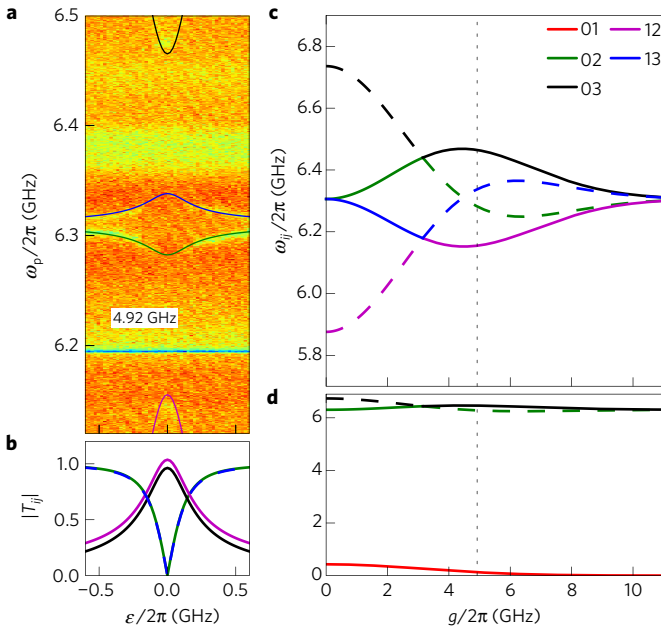

Figure 2 | Transmission spectra for circuits I and II. Calculated transition frequencies ω_{ij}^{cal} are superimposed on the experimental results. As summarized in Table 1, **a** shows data from circuit I at $n_{\phi q} = -0.5$, **b** shows data from circuit I at $n_{\phi q} = -1.5$, **c** shows data from circuit I at $n_{\phi q} = 2.5$, and **d** shows data from circuit II at $n_{\phi q} = -0.5$. The values of $g/2\pi$ are written in the panels. The red, green, blue, and cyan lines indicate the transitions $|0\rangle \to |1\rangle$, $|0\rangle \to |2\rangle$, $|1\rangle \to |3\rangle$, and $|2\rangle \to |4\rangle$, respectively.

as shown in Fig. 3a for circuit I at $n_{\phi q} = -1.5$. As we approach the symmetry point $\varepsilon = 0$, the signals from the $|0\rangle \to |2\rangle$ and $|1\rangle \to |3\rangle$ transitions disappear while the signals from the $|0\rangle \to |3\rangle$ and $|1\rangle \to |2\rangle$ transitions appear near ω_{03}^{cal} and ω_{12}^{cal}. The appearance and disappearance of the signals are well explained by the transition matrix elements $T_{ij} = \langle i|(\hat{a} + \hat{a}^\dagger)|j\rangle$ shown in Fig. 3b: when $\varepsilon \to 0$, $|T_{02}| = |T_{13}| \to 0$ (forbidden transitions), while $|T_{03}|$ and $|T_{12}|$ are maximum (allowed transitions). As can be seen from the expression

Table 1 | Set of parameters obtained from fitting spectroscopy measurements.

Circuit	$n_{\phi q}$	Figure	$\Delta/2\pi$ (GHz)	$\omega_{\text{o}}/2\pi$ (GHz)	$g/2\pi$ (GHz)	$\alpha = g/\omega_{\text{o}}$	$2g/\sqrt{\omega_{\text{o}}\Delta}$
I	−0.5	2a	0.505	6.336	4.57	0.72	5.1
I	−1.5	2b and 3a	0.430	6.306	4.92	0.78	6.0
I	2.5	2c	0.299	6.233	5.79	0.93	8.5
II	−0.5	2d	0.441	5.711	7.63	1.34	9.6
III	0.5	SI6	3.84	5.588	5.63	1.01	2.4

The parameters are obtained from five sets of spectroscopy data in three circuits. The column 'Figure' shows the corresponding figures. 'SI' stands for Supplementary Information.

Figure 3 | Selection rules and transmission spectrum around the symmetry point. a, Transmission spectrum for circuit I at $n_{\phi q} = -1.5$ plotted as a function of flux bias ε. The transition frequencies ω_{ij}^{cal} are superimposed on the experimental result in **a**. **b**, Matrix elements $|T_{ij}|$ calculated using the parameters shown in Table 1, that is, $\Delta/2\pi = 0.430\,\text{GHz}$, $\omega_o/2\pi = 6.306\,\text{GHz}$, and $g/2\pi = 4.92\,\text{GHz}$. **c,d**, Calculated transition frequencies around ω_o (**c**) and from the ground state (**d**) are plotted as functions of g at $\varepsilon = 0$. The red, green, black, magenta, and blue lines in all four panels indicate the transitions $|0\rangle \to |1\rangle$, $|0\rangle \to |2\rangle$, $|0\rangle \to |3\rangle$, $|1\rangle \to |2\rangle$, and $|1\rangle \to |3\rangle$, respectively. Solid (dashed) lines in **c** and **d** indicate that the corresponding matrix elements T_{ij} are nonzero (zero). Allowed and forbidden transitions cross at $g/2\pi \simeq \omega_o/4\pi = 3.15\,\text{GHz}$ (ref. 25), where there is an energy-level crossing and the energy eigenstates $|2\rangle$ and $|3\rangle$ exchange their physical states. The black dotted line is at the coupling strength in circuit I at $n_{\phi q} = -1.5$, $g/2\pi = 4.92\,\text{GHz}$.

for T_{ij}, these features are directly related to the form of the energy eigenstates and can therefore serve as indicators of the symmetry properties of the energy eigenstates, similarly to how atomic forbidden transitions are related to the symmetry of atomic wavefunctions. The weakness of the signals from the $|0\rangle \to |3\rangle$ and $|1\rangle \to |2\rangle$ transitions is probably due to dephasing caused by flux fluctuations. No signals from the $|0\rangle \to |3\rangle$ and $|1\rangle \to |2\rangle$ transitions were observed in circuit I at $n_{\phi q} = 2.5$ and in circuit II. The broad dips at $\omega_p/2\pi = 6.2$, 6.38 and 6.45 GHz are the result of a background frequency dependence of the transmission line's transmission amplitude, and these features can be ignored here. The feature at 6.2 GHz also contains a narrow signal from another qubit–oscillator circuit that is coupled to the transmission line (see Supplementary Section 3).

To conclude this analysis of the observed transmission spectra, the fact that the frequencies of the spectral lines and the points where they become forbidden follow, respectively, ω_{ij}^{cal} and $|T_{ij}|$ lends strong support to the conclusion that $\mathcal{H}_{total}$ accurately describes our circuits. Importantly, in circuits II and III, g is larger than both ω_o and Δ, emphasizing that the circuits are in the deep strong coupling regime [$g \gtrsim \max(\omega_o, \sqrt{\Delta\omega_o}/2)$] (ref. 25). The fact that at $\varepsilon = 0$ the two forbidden transitions are located between the two allowed transitions is a further sign that $g > \omega_o/2$ (see Fig. 3c). In contrast, the highest coupling strengths achieved in previous experiments[12,13] give $g/\omega_o = 0.12$ and 0.1, respectively. From the spectrum in Fig. 3a, we find that $\omega_{01}(\varepsilon = 0)/\Delta = 0.13\,\text{GHz}/0.43\,\text{GHz} = 0.30$, meaning that the Lamb shift[26] is 70% of the bare qubit frequency. The

Table 2 | The energy eigenstates of the qubit–oscillator system.

Energy eigenbasis		$|\text{qubit}\rangle \otimes |\text{oscillator}\rangle$ basis	
$g < \frac{\omega_o}{2}$　　$g > \frac{\omega_o}{2}$		Arbitrary g	$g = 0$
$|0\rangle$	$|0\rangle$	$(|L\rangle_q \otimes |-\alpha\rangle_o + |R\rangle_q \otimes |\alpha\rangle_o)/\sqrt{2}$	$|g\rangle_q \otimes |0\rangle_o$
$|1\rangle$	$|1\rangle$	$(|L\rangle_q \otimes |-\alpha\rangle_o - |R\rangle_q \otimes |\alpha\rangle_o)/\sqrt{2}$	$|e\rangle_q \otimes |0\rangle_o$
$|2\rangle$	$|3\rangle$	$(|L\rangle_q \otimes \hat{D}(-\alpha)|1\rangle_o + |R\rangle_q \otimes \hat{D}(\alpha)|1\rangle_o)/\sqrt{2}$	$|g\rangle_q \otimes |1\rangle_o$
$|3\rangle$	$|2\rangle$	$(|L\rangle_q \otimes \hat{D}(-\alpha)|1\rangle_o - |R\rangle_q \otimes \hat{D}(\alpha)|1\rangle_o)/\sqrt{2}$	$|e\rangle_q \otimes |1\rangle_o$

The left two columns are written in the energy eigenbasis while the right two columns are written in the tensor product basis of qubit and oscillator states. At $g \simeq \omega_o/2$, there is an energy-level crossing and the energy eigenstates $|2\rangle$ and $|3\rangle$ exchange their physical states. $|L\rangle_q$ and $|R\rangle_q$ are the persistent-current states of the qubit, $|g\rangle_q$ and $|e\rangle_q$ are the energy eigenstates of the qubit, $|\pm\alpha\rangle_o = \hat{D}(\pm\alpha)|0\rangle_o$ are coherent states of the oscillator, $\hat{D}(\alpha)$ is a displacement operator, and $|n\rangle_o$ is a Fock state of the bare oscillator. At $g = 0$ and hence $\alpha = 0$, the energy eigenstates are product states, as shown in the rightmost column. For arbitrary g, the energy eigenstates of the qubit–oscillator system are entangled states.

same value (0.30) is obtained from theoretical calculations for $g/\omega_o = 0.78$.

Using our experimental results, we can make a statement regarding the A^2 term and the superradiance no-go theorem[15] in our set-up. A direct consequence of the no-go theorem is that, provided that the condition of the theorem ($C_{A2} > g/\Delta$) is satisfied, the system parameters will be renormalized such that the experimentally measured parameters will satisfy the inequality $2g/\sqrt{\Delta\omega_o} < 1$ (see Methods). However, in all five cases in our experiment, we find that $2g/\sqrt{\Delta\omega_o} > 1$, with the ratio on the left-hand side ranging from 2.4 to 9.6 (see Table 1). These results demonstrate that the A^2 term in our set-up does not satisfy the condition of the no-go theorem and therefore does not preclude a superradiant state. In fact, we expect that $C_{A2} \ll 1$ as shown in Methods.

The energy eigenstates of the qubit–oscillator system can be understood in the following way. In the absence of coupling, the energy eigenstates are product states where the oscillator is described by a Fock state $|n\rangle_o$ with n plasmons. Because of the coupling to the qubit, the state of the oscillator is displaced in one of two opposite directions depending on the persistent-current state of the qubit[25]: $|L\rangle_q \otimes |n\rangle_o \to |L\rangle_q \otimes \hat{D}(-\alpha)|n\rangle_o$ and $|R\rangle_q \otimes |n\rangle_o \to |R\rangle_q \otimes \hat{D}(\alpha)|n\rangle_o$. Here, $\hat{D}(\alpha) = \exp(\alpha\hat{a}^\dagger - \alpha^*\hat{a})$ is the displacement operator, and α is the displacement. The amount of the displacement is approximately $\pm g/\omega_o$. As the energy eigenstates of an isolated qubit at $\varepsilon = 0$ are superpositions of the persistent-current states, $|g\rangle_q = (|L\rangle_q + |R\rangle_q)/\sqrt{2}$ and $|e\rangle_q = (|L\rangle_q - |R\rangle_q)/\sqrt{2}$, the energy eigenstates of the qubit–oscillator system at $\varepsilon = 0$ are well described by Schrödinger-cat-like entangled states between persistent-current states of the qubit and displaced Fock states of the oscillator $\hat{D}(\pm\alpha)|n\rangle_o$, as shown in Table 2. Note that the displaced vacuum state $\hat{D}(\alpha)|0\rangle_o$ is the coherent state $|\alpha\rangle_o = \exp(-|\alpha|^2/2)\sum_{n=0}^{\infty}\alpha^n/\sqrt{n!}|n\rangle_o$. Although the above picture works best when $\omega_o \gg \Delta$, theoretical calculations show that it also gives a rather accurate description for circuit III (with $\omega_o/\Delta = 1.44$) (see Methods). The vanishing of the spectral lines corresponding to the $|0\rangle \to |2\rangle$ and $|1\rangle \to |3\rangle$ transitions at $\varepsilon = 0$ is a consequence of the symmetric form of the energy eigenstates. This symmetry is expected from the current-inversion symmetry in the Hamiltonian $\mathcal{H}_{total}$, and it supports the theoretical prediction that the energy eigenstates at that point are qubit–oscillator entangled states.

Using $\mathcal{H}_{total}$ and the parameters shown in Table 1, we can calculate the qubit–oscillator ground-state entanglement $\mathcal{E}_{gs}$ (see Supplementary Section 5). In all cases, $\mathcal{E}_{gs} \gtrsim 90\%$, and for circuit II in particular $\mathcal{E}_{gs} = 99.88\%$. In comparison, the ground-state entanglement for the parameters of refs 12 and 13 is 6% and 4%, respectively. It should be noted here that in all five cases in our experiment there will be a significant population in the state $|1\rangle$ in thermal equilibrium, and the thermal-equilibrium qubit–oscillator entanglement will be reduced to below 8% for circuits I and II, and 25% for circuit III (see Supplementary Table 1).

In conclusion, we have experimentally achieved deep strong coupling between a superconducting flux qubit and an LC oscillator. Our results are consistent with the theoretical prediction that the energy eigenstates are Schrödinger-cat-like entangled states between persistent-current states of the qubit and displaced Fock states of the oscillator. We have also observed a huge Lamb shift, 70% of the bare qubit frequency. The tiny Lamb shift in natural atoms, which arises from weak vacuum fluctuations, was one of the earliest phenomena to stimulate the study of quantum electrodynamics. Now we can design artificial systems with light–matter interaction so strong that instead of speaking of vacuum fluctuations we speak of a strongly correlated light–matter ground state, defining a new state of matter and opening prospects for applications in quantum technologies.

Note added in proof: After acceptance of our paper, we became aware of a related manuscript[27] taking a different approach to the same theme.

Methods

Methods, including statements of data availability and any associated accession codes and references, are available in the online version of this paper.

References

1. Wineland, D. J. & Itano, W. M. Spectroscopy of a single Mg+ ion. *Phys. Lett. A* **82,** 75–78 (1981).
2. Haroche, S. & Raimond, J. M. Cavity quantum electrodynamics. *Sci. Am.* **268,** 54–60 (1993).
3. Brune, M. *et al*. Quantum Rabi oscillation: a direct test of field quantization in a cavity. *Phys. Rev. Lett.* **76,** 1800–1803 (1996).
4. Raimond, J. M., Brune, M. & Haroche, S. Manipulating quantum entanglement with atoms and photons in a cavity. *Rev. Mod. Phys.* **73,** 565–582 (2001).
5. Mabuchi, H. & Doherty, A. C. Cavity quantum electrodynamics: coherence in context. *Science* **298,** 1372–1377 (2002).
6. Walls, D. F. & Milburn, G. J. *Quantum Optics* (Springer Science & Business Media, 2007).
7. Nakamura, Y., Pashkin, Yu. A. & Tsai, J. S. Coherent control of macroscopic quantum states in a single-Cooper-pair box. *Nature* **398,** 786–788 (1999).
8. Clarke, J. & Wilhelm, F. K. Superconducting quantum bits. *Nature* **453,** 1031–1042 (2008).
9. Chiorescu, I. *et al*. Coherent dynamics of a flux qubit coupled to a harmonic oscillator. *Nature* **431,** 159–162 (2004).
10. Wallraff, A. *et al*. Strong coupling of a single photon to a superconducting qubit using circuit quantum electrodynamics. *Nature* **431,** 162–167 (2004).
11. Devoret, M., Girvin, S. & Schoelkopf, R. Circuit-QED: how strong can the coupling between a Josephson junction atom and a transmission line resonator be? *Ann. Phys.* **16,** 767–769 (2007).
12. Niemczyk, T. *et al*. Circuit quantum electrodynamics in the ultrastrong-coupling regime. *Nat. Phys.* **6,** 772–776 (2010).
13. Forn-Diaz, P. *et al*. Observation of the Bloch-Siegert shift in a qubit-oscillator system in the ultrastrong coupling regime. *Phys. Rev. Lett.* **105,** 237001 (2010).
14. Hepp, K. & Lieb, E. H. On the superradiant phase transition for molecules in a quantized radiation field: the Dicke Maser model. *Ann. Phys.* **76,** 360–404 (1973).
15. Rzążewski, K., Wódkiewicz, K. & Żakowicz, W. Phase transitions, two-level atoms, and the A^2 term. *Phys. Rev. Lett.* **35,** 432–434 (1975).
16. Nataf, P. & Ciuti, C. No-go theorem for superradiant quantum phase transitions in cavity QED and counter-example in circuit QED. *Nat. Commun.* **1,** 72 (2010).
17. Viehmann, O., von Delft, J. & Marquardt, F. Superradiant phase transitions and the standard description of circuit QED. *Phys. Rev. Lett.* **107,** 113602 (2011).
18. Mooij, J. E. *et al*. Josephson persistent-current qubit. *Science* **285,** 1036–1039 (1999).
19. Rabi, I. I. Space quantization in a gyrating magnetic field. *Phys. Rev.* **51,** 652–654 (1937).
20. Shimoda, K., Wang, T. C. & Townes, C. H. Further aspects of maser theory. *Phys. Rev.* **102,** 1308–1321 (1956).
21. Jaynes, E. T. & Cummings, F. W. Comparison of quantum and semiclassical radiation theories with application to the beam maser. *Proc. IEEE* **51,** 89–109 (1963).
22. Braak, D. Integrability of the Rabi model. *Phys. Rev. Lett.* **107,** 100401 (2011).
23. Bourassa, J. *et al*. Ultrastrong coupling regime of cavity QED with phase-biased flux qubits. *Phys. Rev. A* **80,** 032109 (2009).
24. Casanova, J., Romero, G., Lizuain, I., Garca-Ripoll, J. J. & Solano, E. Deep strong coupling regime of the Jaynes-Cummings model. *Phys. Rev. Lett.* **105,** 263603 (2010).
25. Ashhab, S. & Nori, F. Qubit-oscillator systems in the ultrastrong-coupling regime and their potential for preparing nonclassical states. *Phys. Rev. A* **81,** 042311 (2010).
26. Lamb, W. E. & Retherford, R. C. Fine structure of the hydrogen atom by a microwave method. *Phys. Rev.* **72,** 241–243 (1947).
27. Forn-Díaz, P. *et al*. Ultrastrong coupling of a single artificial atom to an electromagnetic continuum in the nonperturbative regime. *Nat. Phys.* http://dx.doi.org/10.1038/nphys3905 (2016).

Author contributions

All authors contributed extensively to the work presented in this paper. F.Y., T.F. and K.S. carried out measurements and data analysis on the coupled flux qubit–LC-oscillator system. F.Y. and T.F. designed and F.Y., T.F. and K.K. fabricated the flux qubit and associated devices. T.F., F.Y., K.K., S.S. and K.S. designed and developed the measurement system. S.A. provided theoretical support and analysis. F.Y., T.F., S.A. and K.S. wrote the manuscript, with feedback from all authors. K.S. designed and supervised the project.

Additional information

Supplementary information is available in the online version of the paper. Reprints and permissions information is available online at www.nature.com/reprints. Correspondence and requests for materials should be addressed to F.Y., T.F., S.A. or K.S.

Competing financial interests

The authors declare no competing financial interests.

Methods

Laser microscope image. The laser microscope image in Fig. 1b was obtained by a Keyence VK-9710 Color 3D Laser Scanning Microscope. The magnification of the objective lens is 10. The application 'VK Viewer' was used for image acquisition.

Scanning electron microscope image. The scanning electron microscope image in Fig. 1c was obtained by a JEOL JIB-4601F. The acceleration voltage was 10 kV, the magnification was 6,500, and the working distance was 8.7 mm.

Nonlinearity of M and the A^2 term of the total Hamiltonian. We now consider the nonlinearity of the mutual inductance M between the flux qubit and the LC oscillator. As discussed in the Supplementary Information, M is almost the same as L_c in Fig. 1a, which depends on the current flowing through the Josephson junction I_b as $L_c(I_b) = \Phi_0/(2\pi\sqrt{(a_cI_c)^2 - I_b^2})$, where $a_cI_c \equiv I_{cM}$ is the critical current of the Josephson junction. We thus assume that M can similarly be written as

$$M(I_b) = \frac{\Phi_0}{2\pi\sqrt{I_{cM}^2 - I_b^2}} \tag{2}$$

The nonlinearity of $M(I_b)$ up to second order in δI_b can be written as

$$M(I_b + \delta I_b) = M(I_b) + \delta I_b \frac{\partial M(I_b)}{\partial I_b} + \frac{\delta I_b^2}{2} \frac{\partial^2 M(I_b)}{\partial I_b^2}$$

$$= M(I_b) \left(1 + \frac{I_b \delta I_b}{I_{cM}^2 - I_b^2} + \frac{I_{cM}^2 + 2I_b^2}{2(I_{cM}^2 - I_b^2)^2} \delta I_b^2\right) \tag{3}$$

The coupling Hamiltonian can be written as $\mathcal{H}_c = M(\hat{I}_q + \hat{I}_o)\hat{I}_q\hat{I}_o = M(\hat{I}_q + \hat{I}_o)I_p\sigma_z I_{zpf}(\hat{a} + \hat{a}^\dagger)$, where $\hat{I}_q = I_p\sigma_z$ is the persistent-current operator of the qubit, $\hat{I}_o = I_{zpf}(\hat{a} + \hat{a}^\dagger)$ is the current operator of the oscillator, and the current $\hat{I}_q + \hat{I}_o$ flows through the mutual inductance. Typically, $I_p \gg I_{zpf}$. Taking into account the nonlinearity of $M(\hat{I}_q + \hat{I}_o)$, the coupling Hamiltonian is written as

$$\mathcal{H}_c = M(\hat{I}_q + \hat{I}_o)\hat{I}_q\hat{I}_o$$

$$= M(\hat{I}_q) \left(1 + \frac{\hat{I}_q\hat{I}_o}{I_{cM}^2 - \hat{I}_q^2} + \frac{I_{cM}^2 + 2\hat{I}_q^2}{2(I_{cM}^2 - \hat{I}_q^2)^2}\hat{I}_o^2\right)\hat{I}_q\hat{I}_o$$

$$= M(I_p)\left[I_pI_{zpf}\sigma_z(\hat{a} + \hat{a}^\dagger) + \frac{I_p^2I_{zpf}^2}{I_{cM}^2 - I_p^2}(\hat{a} + \hat{a}^\dagger)^2 + \frac{(I_{cM}^2 + 2I_p^2)I_pI_{zpf}^3}{2(I_{cM}^2 - I_p^2)^2}\sigma_z(\hat{a} + \hat{a}^\dagger)^3\right]$$

$$= \hbar g[\sigma_z(\hat{a} + \hat{a}^\dagger) + C_{A2}(\hat{a} + \hat{a}^\dagger)^2 + C_{A3}\sigma_z(\hat{a} + \hat{a}^\dagger)^3] \tag{4}$$

where

$$\hbar g = M(I_p)I_pI_{zpf} \tag{5}$$

$$C_{A2} = \frac{I_pI_{zpf}}{I_{cM}^2 - I_p^2} \tag{6}$$

and

$$C_{A3} = \frac{(I_{cM}^2 + 2I_p^2)I_{zpf}^2}{2(I_{cM}^2 - I_p^2)^2} \tag{7}$$

Here, we considered terms up to second order in I_{zpf}/I_p. We find that $1 \gg C_{A2} \gg C_{A3}$ considering the following relation, $I_{cM}(= a_cI_c) > I_p(\lesssim a_3I_c) \gg I_{zpf}(\ll I_c)$, where $a_c \gtrsim 1$, $0.4 \lesssim a_3 \lesssim 0.8$, I_c is several hundred nanoamperes, and I_{zpf} is several tens of nanoamperes (see Supplementary Section 2). Since the term C_{A3} is very small, we ignore the third term in equation (4).

The total Hamiltonian of the circuit considering the nonlinearity of M up to first order in I_{zpf}/I_p is given by

$$\mathcal{H}_{total} = -\frac{\hbar}{2}(\Delta\sigma_x + \varepsilon\sigma_z) + \hbar\omega_o\left(\hat{a}^\dagger\hat{a} + \frac{1}{2}\right) + \hbar g\sigma_z(\hat{a} + \hat{a}^\dagger) + C_{A2}\hbar g(\hat{a} + \hat{a}^\dagger)^2 \tag{8}$$

where the first term is the Hamiltonian of the flux qubit, the second term is the Hamiltonian of the LC oscillator, and the third term is the coupling Hamiltonian.

The fourth term proportional to $(\hat{a} + \hat{a}^\dagger)^2$ is known as the A^2 term in atomic physics. This term can be eliminated by a variable transformation as

$$\mathcal{H}_{total} = -\frac{\hbar}{2}(\Delta\sigma_x + \varepsilon\sigma_z) + \hbar\omega_o\left(\hat{a}^\dagger\hat{a} + \frac{1}{2}\right) + C_{A2}\hbar g(\hat{a} + \hat{a}^\dagger)^2 + \hbar g\sigma_z(\hat{a} + \hat{a}^\dagger)$$

$$= -\frac{\hbar}{2}(\Delta\sigma_x + \varepsilon\sigma_z) + \left(\frac{\hbar\omega_o}{4} + C_{A2}\hbar g\right)(\hat{a} + \hat{a}^\dagger)^2 - \frac{\hbar\omega_o}{4}(\hat{a} - \hat{a}^\dagger)^2 + \hbar g\sigma_z(\hat{a} + \hat{a}^\dagger)$$

$$= -\frac{\hbar}{2}(\Delta\sigma_x + \varepsilon\sigma_z) + \frac{\hbar\omega_o'}{4}(\hat{b} + \hat{b}^\dagger)^2 - \frac{\hbar\omega_o'}{4}(\hat{b} - \hat{b}^\dagger)^2 + \hbar g'\sigma_z(\hat{b} + \hat{b}^\dagger)$$

$$= -\frac{\hbar}{2}(\Delta\sigma_x + \varepsilon\sigma_z) + \hbar\omega_o'\left(\hat{b}^\dagger\hat{b} + \frac{1}{2}\right) + \hbar g'\sigma_z(\hat{b} + \hat{b}^\dagger) \tag{9}$$

where

$$\omega_o' = \sqrt{\omega_o^2 + 4C_{A2}g\omega_o} \tag{10}$$

$$g' = \sqrt{\frac{\omega_o}{\omega_o'}}g \tag{11}$$

and the new field operators,

$$\hat{b} + \hat{b}^\dagger = \sqrt{\frac{\omega_o'}{\omega_o}}(\hat{a} + \hat{a}^\dagger) \tag{12}$$

and

$$\hat{b} - \hat{b}^\dagger = \sqrt{\frac{\omega_o}{\omega_o'}}(\hat{a} - \hat{a}^\dagger) \tag{13}$$

are used. The form of the Hamiltonian in equation (9) is exactly the same as the one where the coupling term is linear in $(\hat{a} + \hat{a}^\dagger)$, which is given by

$$\mathcal{H}_{total}^{linear} = -\frac{\hbar}{2}(\Delta\sigma_x + \varepsilon\sigma_z) + \hbar\omega_o\left(\hat{a}^\dagger\hat{a} + \frac{1}{2}\right) + \hbar g\sigma_z(\hat{a} + \hat{a}^\dagger) \tag{14}$$

Note that the transformation described by equations (12) and (13) is a Hopfield–Bogoliubov transformation[28]. It guarantees that $[\hat{b}, \hat{b}^\dagger] = [\hat{a}, \hat{a}^\dagger] = 1$. In other words, both the $\hat{a}$ operators and the $\hat{b}$ operators obey the harmonic oscillator commutation relations. The two sets of operators are related to each other by quadrature squeezing operations. The most natural choice among these two and all other quadrature-squeezed variants is the one that leads to the standard form of the harmonic oscillator Hamiltonian, usually expressed as $\hbar\omega_o\hat{a}^\dagger\hat{a}$. As such, the $\hat{b}$ operators are the most natural oscillator operators for our circuits. The $\hat{a}$ operators were defined based on an incomplete description of the circuit, considering the properties of the LC circuit and ignoring the qubit and coupler parts of the circuit. In particular, the A^2 term in our circuits describes an additional contribution to the inductive energy of the oscillator that arises in the presence of the qubit and coupler circuits. Similarly, the expression given in the main text for the current zero-point fluctuations must be modified in order to correctly describe the fluctuations in the full circuit.

Condition for superradiant phase transition. In cases where one expects a sharp transition from a normal to a superradiant state, for example, when $\Delta \gg \omega_o$ or when the single qubit is replaced by a large ensemble of N qubits (and g is defined to include the ensemble enhancement factor $\sqrt{N}$), the phase transition condition (without the A^2 term) is:

$$4g^2 = \Delta \times \omega_o \tag{15}$$

After taking into account the renormalization of ω_o and g caused by the A^2 term as described above, the condition for the phase transition becomes

$$4g^2\sqrt{\frac{\omega_o}{\omega_o + 4C_{A2}g}} = \Delta \times \omega_o \times \sqrt{\frac{\omega_o + 4C_{A2}g}{\omega_o}} \tag{16}$$

or in other words

$$4g^2 = \Delta \times (\omega_o + 4C_{A2}g) \tag{17}$$

If the parameters are constrained to satisfy the relation $C_{A2} > g/\Delta$, the right-hand side increases whenever we increase the left-hand side, and no matter how large g becomes it will never be strong enough to satisfy the phase transition condition. This can indeed be the case with atomic qubits, and it leads to the no-go theorem in those systems[15].

Fidelities of qubit–oscillator entangled states for circuit III. The fidelity between two pure states $|\phi\rangle$ and $|\psi\rangle$ is given by $F(|\phi\rangle, |\psi\rangle) = |\langle\phi|\psi\rangle|^2$. For circuit III, the fidelities between the four lowest energy eigenstates given in Table 2 $|i_{\text{TII}}\rangle$ and the corresponding exact energy eigenstates of $\mathcal{H}_{\text{total}}|i_{\text{exact}}\rangle$ ($i = 0, 1, 2, 3$) are calculated to be $F(|0_{\text{TII}}\rangle, |0_{\text{exact}}\rangle) = 0.981$, $F(|1_{\text{TII}}\rangle, |1_{\text{exact}}\rangle) = 0.985$, $F(|2_{\text{TII}}\rangle, |2_{\text{exact}}\rangle) = 0.975$, and $F(|3_{\text{TII}}\rangle, |3_{\text{exact}}\rangle) = 0.967$. All the other data sets give significantly higher fidelities. In particular, for circuit II $F(|0_{\text{TII}}\rangle, |0_{\text{exact}}\rangle) = 0.99994$.

References

28. Hopfield, J. J. Theory of the contribution of excitons to the complex dielectric constant of crystals. *Phys. Rev.* **112,** 1555–1567 (1958).